A modified space vector modulation based rotor flux oriented control of six-phase asymmetrical induction motor drive

Krunal SHAH, Rakesh MAURYA*

Department of Electrical Engineering, Sardar Vallabhbhai National Institute of Technology, Surat, India

Abstract: In view of the attractive features like improved torque density, reduction torque pulsation, superior fault tolerance, reduced power rating of voltage source converter, and sterling noise characteristics of six-phase asymmetrical induction motor (SPAIM) as compared to its three-phase counterpart, the SPAIM is considered for the study. In this paper, mathematical modelling of SPAIM is carried out in the synchronous reference frame and then indirect rotor field-oriented control (IRFOC) of SPAIM using a modified carrier wave-based space vector modulation (SVM) scheme is developed. A Simulink model of the proposed system configuration is developed and a simulation study is carried out. In order to validate the simulation results, a scaled prototype model of SPAIM rated for 2 HP, 4-pole, 200V is developed, and closed loop control of SPAIM drive with aforesaid modified SVM technique is implemented using TMS320F28379D controller board. The performance of the system is observed in several operating conditions with simulation studies using MATLAB/Simulink and test setup and various test results are recorded under several operating conditions and presented. Furthermore, the proposed SVM technique is compared with benchmarked SPWM and hysteresis current controller as well and it is observed that it outperforms traditional SPWM and hysteresis-based current controllers in terms of the distortion of stator currents and torque ripples.

Key words: Multiphase induction motor, modified SVM, direct torque control (DTC), IRFOC

1. Introduction

The three-phase induction motor (TPIM) drives are widely used in various industrial applications because of their robust structure, low cost, and high reliability. However, the TPIM is unsuitable in a few applications where high redundancy and reliability are required, even under a fault condition. In several industrial applications and transportation frameworks such as electric cars, propulsion systems of electrical locomotives, and electrical ships, the multiphase induction motor (MPIM) drive can be an alternate choice of the TPIM drive because of certain advantages like higher torque density, reduced torque pulsation, higher reliability under fault condition, requires less dc-link voltage, and lower copper losses in the stator [1–10]. In the year 1969, the five-phase IM was introduced as a MPIM drive to reduce torque ripple compared to three-phase machines [4, 5]. Though it was operated initially with a square wave, later on, various PWM techniques were introduced. Simultaneously, multiphase machines particularly, the SPAIM is evolved with various attractive features like reduced per phase rating of the converter, without increasing per phase voltage and current. The SPAIM drive also finds its utilization in safety-critical applications such as more electric aircraft due to its superior fault tolerance capability. It has been reported that the drive behaviour was affected trivially by the fault in one or two

---

*Correspondence: rmaurya@eed.svnit.ac.in

phases [7–9]. In high-power applications (typically over 100kWs), the employment of SPAIM drive facilitates the reduction in per phase power requirements. Moreover, as it can be handled with a reduced power rating of switches, this is most blissful over the converter end. Conventionally, a large amount of power is processed with various combinations of the switch, which causes problems in the static and dynamic sharing of voltage as well as current. Thus, it is an appealing solution to have a reduction in per phase power.

The general concept of mathematical modelling of induction motor with n-number of phases on both stator and rotor has been discussed in Levi et al. [4] and Bojoi et al. [5]. The detailed modelling of a SPAIM has been mentioned in Krause et al. [3].

In the literature, various carrier-based PWM (CPWM) techniques and space vector PWM (SVPWM) have been proposed for a six-phase two-level voltage source inverter (SPTL-VSI) to overcome several control-related issues. The CPWM technique is simple and easy to implement with lower computational costs. On the other hand, SVPWM technique is superior to CPWM in terms of output power quality, common-mode voltage (CMV), switching losses, and fault-tolerant capability. Usually, the stator currents of the SPAIM drive contain harmonic components depending upon the PWM technique used. These harmonic components increase losses in the stator winding and thereby cause heating in the motor windings. Therefore, many researchers focused on the research area of developing the appropriate PWM scheme to reduce stator current distortions [11–13]. In literature, several space vector modulation techniques have been proposed to improve the MPIM drive's performance without changing the design of motor. Different continuous and discontinuous PWM techniques have been analysed and 24 sector-based SVPWM technique for SPAIM has been proposed [11]. In [12], various pulse width modulation techniques have been compared regarding various performance parameters, such as HDF and stator current THD. The various PWM techniques with reduced stator current distortion features have been analysed in [13]. However, all these modulation techniques have been evaluated and tested under open-loop operation and need to be further tested and verified with closed-loop control of the SPAIM drive.

Various control techniques such as indirect field-oriented control (IRFOC), switching table-based direct torque control (ST-DTC), and predictive torque control (PTC) have been extended to control the SPAIM drives [14–25]. For the IRFOC of the SPAIM drive, the six-phase variables are converted into d-q, x-y, and 01-02 subspaces using the vector space decomposition (VSD) approach as presented in [6]. Only the current components from the d-q subspace are responsible for torque generation. The current components of the x-y subspace are responsible for losses in the machine. Therefore, the major issue to be considered while using FOC with SPAIM is the reduction of stator current distortion. This can be achieved by reducing current components in the x-y subspace. The capability to restrain stator current harmonics is reduced due to the reduced stator resistance value and leakage reactance in the SPAIM drive compared to its three-phase counterpart [6]. The various aspects of ST-DTC are documented in the literature compared to other techniques [15, 16]. The synthetic voltage vector-based direct torque for SPAIM to reduce stator current distortion has been represented in Pandit et al. [14] and Shaikh et al. [15]. Shao et al. [16] present ST-DTC with selective harmonics elimination from stator current for multiphase PMSM drive. ST-DTC scheme with reduced torque ripples is represented in [17]. The ST-DTC provides a fast dynamic response but also increases the torque ripples and stator current distortion. The IRFOC outperforms stator current distortion, torque ripples, and constant switching frequency compared to ST-DTC. To overcome these limitations of ST-DTC, field-oriented control (FOC) can be an interesting alternative. The FOC emulates features of DC-motor control by proper orientation of the rotor flux. For the high-performance control of induction motor drive, the IRFOC is viewed as one of the most powerful methods.

In literature, many researchers present IRFOC for multiphase drives. Digital field-oriented control of SPAIM is represented in [18, 19]. The IRFOC with sine pulse width modulation (SPWM) for five-phase motors has been presented in [20]. The IRFOC for a five-phase induction motor has been designed and developed using the synchronous current control method by Jones et al. [21]. The modular vector control of a multiphase PMSM motor has been discussed in [22]. The various algorithms of current sharing for decoupled control of multiphase induction motor drive have been compared in [23]. The sensor-less IRFOC with the parallel estimation of rotor time constant and speed is proposed by Holakooie et al. [24]. The modular control of stator flux and torque for multiphase induction motors has been proposed by Rubino et al. [25].

In this work, the IRFOC of SPAIM drive is carried out using a modified carrier-based SVM technique using only two PI current controllers and its closed-loop control is implemented using TMS320F28379D controller board, and its performances are analysed. Further, a comparative study with benchmarked IRFOC schemes based on hysteresis current controllers and SPWM techniques is carried out. Based on the study, it is observed that SPWM technique suffers from the problem of higher distortion of current and higher ripple content in torque. Whereas, with the utilization of the modified SVM technique, the distortion of the stator currents of SPAIM is reduced to a greater extent.

The overall manuscript is organized into six sections. Section 1 presents the key applications, issues, and challenges of multi-phase machines. It also presents brief literature reviews highlighting the advanced control methodologies for SPAIM drives. The mathematical modelling of a SPAIM is carried out in Section 2. It covers the general configuration of the SPAIM drive and the mathematical formulation required for developing the Simulink model of the machine. Section 3 presents the basic concept of IRFOC strategy and details about the modified carrier-based SVM technique. The development of a laboratory-scaled prototype of the SPAIM drive, along with results and discussion, is presented in section 4. The comparison of various FOC methods has been carried out regarding stator current distortion, torque ripples, and computational complexity in section 5. Finally, the outcome of the research work is summarized in Section 6.

2. Mathematical modelling and system configuration

The configuration of the SPAIM drive is shown in Figure 1. The schematic diagram of the SPAIM drive system includes SPAIM, a SPTL-VSI, and an IRFOC scheme. The SPAIM is powered by six legs IGBT based VSI. The DC link voltage of SPTL-VSI is maintained constant. The speed of SPAIM is controlled by the IRFOC scheme and the gate pulses are generated by a modified 24 sector-based space vector modulation technique. The following subsections describe the system configuration in detail.

The analysis and control of the induction machine can be simplified by imitating it as dc machine using the theory of reference frame. Coordinate transformation along with the help of power invariant form is used for the transformation of phase variables into equivalent $(d - q - 0)$ variables. The following transformation matrix is therefore applied to the stator six-phase winding:

$$T_s = \sqrt{\frac{2}{6}} \begin{bmatrix} 1 & \cos\left(\frac{2\pi}{3}\right) & \cos\left(\frac{4\pi}{3}\right) & \cos\left(\frac{\pi}{6}\right) & \cos\left(\frac{5\pi}{6}\right) & \cos\left(\frac{9\pi}{6}\right) \\ 0 & sin\left(\frac{2\pi}{3}\right) & sin\left(\frac{4\pi}{3}\right) & sin\left(\frac{\pi}{6}\right) & sin\left(\frac{5\pi}{6}\right) & sin\left(\frac{9\pi}{6}\right) \\ 1 & \cos\left(\frac{4\pi}{3}\right) & \cos\left(\frac{8\pi}{3}\right) & \cos\left(\frac{5\pi}{6}\right) & \cos\left(\frac{\pi}{6}\right) & \cos\left(\frac{9\pi}{6}\right) \\ 0 & sin\left(\frac{4\pi}{3}\right) & sin\left(\frac{8\pi}{3}\right) & sin\left(\frac{5\pi}{6}\right) & sin\left(\frac{\pi}{6}\right) & sin\left(\frac{9\pi}{6}\right) \\ 1 & 1 & 1 & 0 & 0 & 0 \\ 0 & 0 & 0 & 1 & 1 & 1 \end{bmatrix} \tag{1}$$
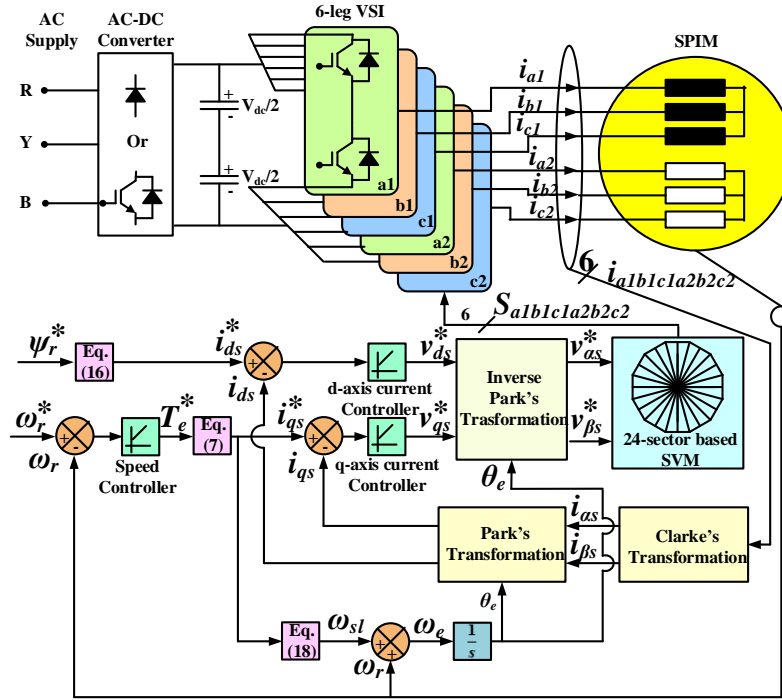
Figure 1. Schematic block diagram of SPAIM drive.

$$
T_s^{-1} = \sqrt{\frac{2}{6}}
\begin{bmatrix}
1 & 0 & 1 & 0 & 1 & 0 \\
\cos\left(\frac{2\pi}{3}\right) & \sin\left(\frac{2\pi}{3}\right) & \cos\left(\frac{4\pi}{3}\right) & \sin\left(\frac{4\pi}{3}\right) & 1 & 0 \\
\cos\left(\frac{4\pi}{3}\right) & \sin\left(\frac{4\pi}{3}\right) & \cos\left(\frac{8\pi}{3}\right) & \sin\left(\frac{8\pi}{3}\right) & 1 & 0 \\
\cos\left(\frac{\pi}{6}\right) & \sin\left(\frac{\pi}{6}\right) & \cos\left(\frac{5\pi}{6}\right) & \sin\left(\frac{5\pi}{6}\right) & 0 & 1 \\
\cos\left(\frac{5\pi}{6}\right) & \sin\left(\frac{5\pi}{6}\right) & \cos\left(\frac{\pi}{6}\right) & \sin\left(\frac{\pi}{6}\right) & 0 & 1 \\
\cos\left(\frac{9\pi}{6}\right) & \sin\left(\frac{9\pi}{6}\right) & \cos\left(\frac{9\pi}{6}\right) & \sin\left(\frac{9\pi}{6}\right) & 0 & 1
\end{bmatrix}
\tag{2}
$$

The above-mentioned transformation matrices are used for transformation of stator quantities from phase variables to $(d - q - 0)$ variables and vice-versa. The stator windings of the SPAIM are made up of two sets of three-phase star-connected stator winding with 30 degree displaced and rotor is similar to squirrel cage rotor of convention TPIM. The phase-variable model of SPAIM can be represented by using equation (3).

$$
\begin{aligned}
\vec{v}_s &= R_s \vec{i}_s + p\vec{\psi}_s + j\omega_a \vec{\psi}_s \\
\vec{v}_r &= R_r \vec{i}_r + p\vec{\psi}_r + j\left(\omega_a - \omega_r\right)\vec{\psi}_r \\
\vec{\psi}_s &= L_s \vec{i}_s + L_m \vec{i}_r \\
\vec{\psi}_r &= L_r \vec{i}_r + L_m \vec{i}_s
\end{aligned}
\tag{3}
$$

The modelling of motor is carried out by transforming phase variables into three sets of mutually orthogonal variables i.e. $(d - q)$, $(x - y)$, and $(0_+ - 0_-)$. The six-phase voltage supply from the inverter is converted in $(dq0)$ form using Clark's and Park's transformation respectively. The Clarke's transformation

matrix used for six-phase system is given by equation (1),

$$v_{dqs} = T_S v_{abcdefs}$$

$$v_{dqr} = T_S v_{abcdefr}$$

$$i_{dqs} = T_s i_{abcdefs}$$

$$i_{dqr} = T_s i_{abcdefr} \tag{4}$$

$$\psi_{dqs} = T_s \psi_{abcdefs}$$

$$\psi_{dqr} = T_s \psi_{abcdefr}$$

It is possible to eliminate the effect of time-varying inductances by using a typical arbitrary frame of reference rotates at an angular velocity of ωe. By substituting equation (3) in equation (4) and using equation (1), the equations for the flux linkages, voltages of stator and rotor using $(d - q - x - y)$ can be represented as follow, the flux linkages on $(d - q)$ and $(x - y)$ subspace are expressed as follows:

$$\psi_{ds} = (L_m + L_{ls})i_{ds} + L_m i_{dr}$$

$$\psi_{qs} = (L_m + L_{ls})i_{qs} + L_m i_{qr}$$

$$\psi_{dr} = (L_m + L_{ls})i_{dr} + L_m i_{ds}$$

$$\psi_{qr} = (L_m + L_{ls})i_{qr} + L_m i_{qs} \tag{5}$$

$$\psi_{xs} = L_{ls}i_{xs}$$

$$\psi_{ys} = L_{ls}i_{ys}$$

The stator voltages in $(d - q)$ and $(x - y)$ subspaces are represented as given in equation (6).

$$v_{ds} = i_{ds}R_s - \psi_{qs}\omega_a + p\psi_{ds}$$

$$v_{qs} = i_{qs}R_s - \psi_{ds}\omega_a + p\psi_{qs}$$

$$v_{xs} = i_{xs}R_s + p\psi_{xs} \tag{6}$$

$$v_{ys} = i_{ys}R_s + p\psi_{ys}$$

Coupling between stator and rotor is not present in $(x - y)$ plane and hence, the voltage equations for rotor can be given as,

$$v_{dr} = 0 = i_{dr}R_r - \psi_{qr}(\omega_a - \omega_r) + p\psi_{dr}$$

$$v_{qr} = 0 = i_{qr}R_r + \psi_{dr}(\omega_a - \omega_r) + p\psi_{qr} \tag{7}$$

The electromagnetic torque can be given as,

$$T_e = PL_m(i_{qs}i_{dr} - i_{ds}i_{qr}) \tag{8}$$

The mechanical equation of rotor motion is invariant under the transformation and is

$$\omega_r = \int \frac{P}{2J}(T_e - T_L)dt \tag{9}$$

3. Indirect rotor field-oriented control scheme

In the field-oriented control, the stator current is decomposed into two components namely direct axis component (i_{ds}) and quadrature axis component (i_{qs}). The direct axis component is in the direction of flux linkage, and the quadrature axis component is orthogonal to it. The fast dynamics of the response of the motor can be achieved as both the components of the current are controlled individually and independently. An induction motor necessitates only these components of current for torque generation irrespective of the number of phases. For the operation under base speed region (d)-axis current component is maintained constant, but for operation in field weakening mode requires an appropriate reduction in it.

For multiphase motor, the principle of operation for FOC remains the same as that of TPIM as vector control requires only two components of current. The only difference is in the dimension of the matrix used for the transformations of current. In order to simplify the analysis of FOC consider the equivalent $(d-q)$ model of SPAIM shown in Figure 2.
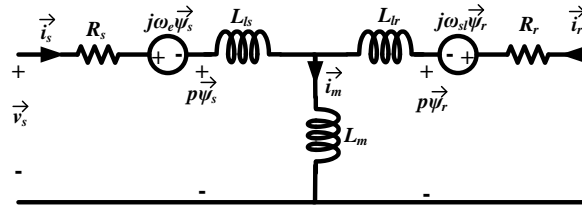

Figure 2. Equivalent circuit of phasor model of the SPAIM.

With reference to the phasor model depicted in Figure 2, the equation (10) is obtained as given below:

$$p\psi_r = -R_r \vec{i_r} - j(\omega_a - \omega_r)\vec{\psi_r} \tag{10}$$

The rotor current, is obtained from equation (3), as given below:

$$\vec{i_r} = \frac{1}{L_m}(\vec{\psi_r} - L_m\vec{i_s}) \tag{11}$$

The equation (10) and equation (11), gives equation (12).

$$p\vec{\psi_r} = -\frac{R_r}{L_r}(\vec{\psi_r} - L_m\vec{i_s}) - j(\omega_a - \omega_r)\vec{\psi_r} \tag{12}$$

After simplification of equation(12), the equation (13) is obtained.

$$\vec{\psi_r}(1 + T_r(p + j(\omega_a - \omega_r))) = L_m\vec{i_s} \tag{13}$$

After decomposing the equation (12) in dq-axis component and considering the orientation of rotor flux ($j\psi_{qr} = 0$ and $\psi_{dr} = \psi_r$), yields the equation (14):

$$\psi_r(1 + pT_r) = L_m i_{ds} \tag{14}$$

$$i_{ds}^* = \frac{\psi_r^*}{L_m}(1 + pT_r) \tag{15}$$

Since during the general operation rotor flux command ψ_r^* remains constant, the simplified i_{ds}^* can be represented from the above equation as follows.

$$i_{ds}^* = \frac{\psi_r^*}{L_m} \tag{16}$$

The relation between rotor flux command ψ_r^* and d-axis current command i_{ds}^* is obtained from the equation (16). The actual speed and commanded speed are compared and the error is regulated with a speed controller (PI regulator) to obtain torque command. In order to achieve rapid acceleration, the output of the speed controller is regulated within the band of rated torque and twice the rated torque. The q-axis current command is determined by multiplying the torque command by constant K_T.

$$i_{qs}^* = K_T T_e^*$$
$$K_T = \frac{L_r}{PL_m\psi_r^*} \tag{17}$$

The slip and rotor position can be calculated as follow,

$$\omega_{sl} = \frac{L_m i_{qs}^*}{T_r \psi_r^*}$$
$$\theta_e = \int (\omega_r + \omega_{sl}) dt \tag{18}$$

The actual and reference values of direct and quadrature axis currents are compared and the error is regulated by d-axis and q-axis current controllers as shown in Figure1. The output of these current controllers will be reference values of d-axis and q-axis voltages. In order to produce the gate pulses, first the direct and quadrature axis reference voltages are converted into the stationary frame reference voltages using the equation (19), and then the α-axis and β-axis voltage commands are processed by 24 sector-based space vector modulation technique to generate gate pulses for the SPTL-VSI.

$$\begin{bmatrix} v_{\alpha s}^* \\ v_{\beta s}^* \\ 0 \end{bmatrix} = \begin{bmatrix} \cos\theta_e & -\sin\theta_e \\ \sin\theta_e & \cos\theta_e \end{bmatrix} \begin{bmatrix} v_{ds}^* \\ v_{qs}^* \\ 0 \end{bmatrix} \tag{19}$$

3.1. Modified space vector modulation scheme

The power circuit of the SPAIM drive comprises of SPTL-VSI with two IGBTs in each leg as depicted in Figure 1. Therefore, 2^6 i.e. 64 possible switching vectors distributed in 24 sectors exist for the operation of the SPTL-VSI as shown in Figure 3. Further, based on their magnitude, these switching vectors are categorized into five groups namely Large (L), Medium Large (ML), Medium (M), Small (S), and Zero (Z) as tabulated in Table 1. In the conventional carrier-based space vector modulation (SVM) technique, the combination of the Large vectors and Zero vectors is utilized for the realization of reference voltage depending upon its position in the sector. The conventional SVM method uses 4 large and 2 zero switching vectors along with one carrier wave for the generation of gate pulses for the SPTL-VSI. In the modified space vector modulation technique, to synthesise the reference voltage vector, a combination of three large, one medium, and one zero switching vectors is utilized. In order to reduce the distortion in stator currents, a modified carrier based SVM technique is used to control the output voltage of SPTL-VSI. The switching vector orientations in $d-q$ and $x-y$ subspace are depicted in Figure 3.
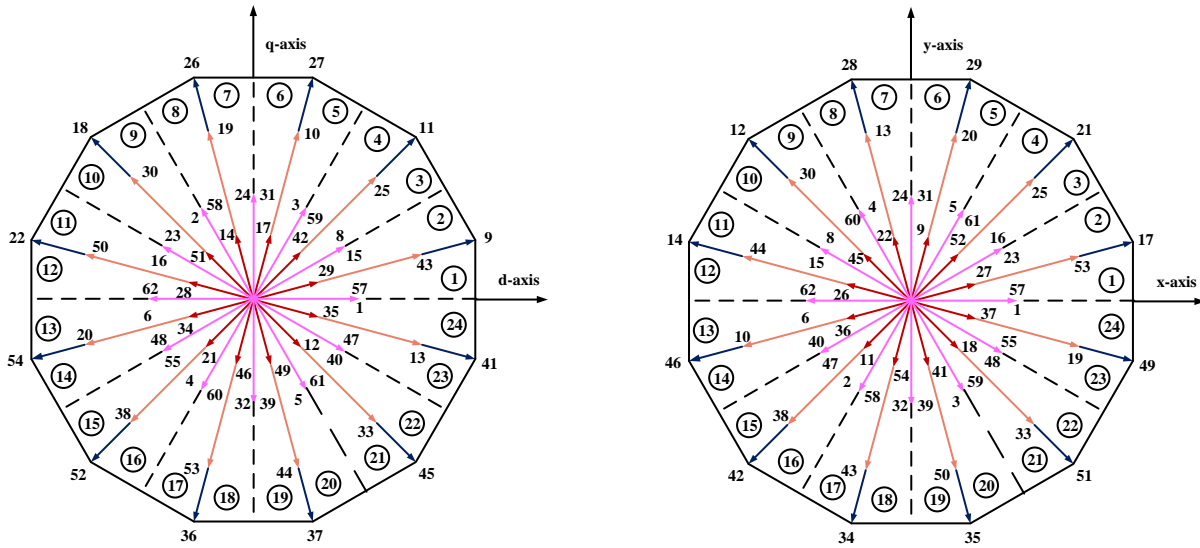
Figure 3. Switching vector orientation in (a) $d - q$ subspace (b) $x - y$ subspace.

Table 1. Classification of switching vectors.

Sr. No.	Types of switching vector	Switching vectors	Quantity
1	Large (L)	27,11,9,41,45,37,36,52,54,22,18,26	12
2	Medium Large (ML)	10,25,43,13,33,44,5,38,20,50,30,9	12
3	Medium (M)	8,15,57,1,40,47,61,5,39,32,60,4, 55,48,6,62,16,23,2,58,24,31,3,59	24
4	Small (S)	17,42,29,35,12,49,46,21,34,28,51,14	12
5	Zero (Z)	7,56,63,0	4
Total number of switching vectors			64

The switching pattern for the first four sectors is shown in Table 2 and based on these switching sequences, the switching sequences for the remaining twenty sectors can be determined.

Table 2. Switching sequences.

Sector	Switching pattern	Application time of voltage vector			
		t1	t2	t3	t4
1	56-40-41-9-11	-T1	-T6	T3	T4
2	41-9-11-3-7	T2	T5	T9	T1
3	0-1-9-11-27	-T6	T3	T8	-T2
4	9-11-27-31-63	T7	T9	T1	T6

In order to calculate the dwell times for any sector, the instantaneous output voltage of SPTL-VSI can be represented using equation (20):

$$\begin{bmatrix} V_a & V_b & V_c & V_d & V_e & V_f \end{bmatrix}^T = [M] \begin{bmatrix} S_a & S_b & S_c & S_d & S_e & S_f \end{bmatrix}^T \tag{20}$$

Where,

$$[M] = \frac{V_{dc}}{3} \begin{bmatrix} 2 & -1 & -1 & 0 & 0 & 0 \\ -1 & 2 & -1 & 0 & 0 & 0 \\ -1 & -1 & 2 & 0 & 0 & 0 \\ 0 & 0 & 0 & 2 & -1 & -1 \\ 0 & 0 & 0 & -1 & 2 & -1 \\ 0 & 0 & 0 & -1 & -1 & 2 \end{bmatrix}$$

The voltage vectors of SPTL-VSI can be transferred into $(d - q)$, $(x - y)$ variables using the matrix given in equation (1). For example, in the given technique for sector 1, active voltage vectors V56, V40, V41, V9, and V11 are computed and transferred into d-q, x-y variables by utilizing equation (20) as follow,

$$\begin{bmatrix} V_{sd40} & V_{sd41} & V_{sd9} & V_{sd11} \\ V_{sq40} & V_{sq41} & V_{sq9} & V_{sq11} \\ V_{sx40} & V_{sx41} & V_{sx9} & V_{sx11} \\ V_{sy40} & V_{sy41} & V_{sy9} & V_{sy11} \end{bmatrix} = \frac{V_{dc}}{2\sqrt{3}} \begin{bmatrix} \sqrt{3} & 2+\sqrt{3} & 2+\sqrt{3} & 1+\sqrt{3} \\ -1 & -1 & 1 & 1+\sqrt{3} \\ -\sqrt{3} & 2-\sqrt{3} & 2-\sqrt{3} & 1-\sqrt{3} \\ -1 & -1 & 1 & 1-\sqrt{3} \end{bmatrix} \tag{21}$$

The dwell times (t1 to t4) for the voltage vectors can be calculated using equation (21).

$$\begin{bmatrix} t_1 \\ t_2 \\ t_3 \\ t_4 \end{bmatrix} = \begin{bmatrix} V_{sd40} & V_{sd41} & V_{sd9} & V_{sd11} \\ V_{sq40} & V_{sq41} & V_{sq9} & V_{sq11} \\ V_{sx40} & V_{sx41} & V_{sx9} & V_{sx11} \\ V_{sy40} & V_{sy41} & V_{sy9} & V_{sy11} \end{bmatrix}^{-1} \begin{bmatrix} V_{sd}^* T_s \\ V_{sq}^* T_s \\ V_{sx}^* T_s \\ V_{sy}^* T_s \end{bmatrix} \tag{22}$$

The substituting equation (21) in equation (22) and $V_{sx}^* = V_{sy}^* = 0$, then the dwell times can be calculated as follows,

$$\begin{bmatrix} t_1 \\ t_2 \\ t_3 \\ t_4 \end{bmatrix} = \begin{bmatrix} \frac{T_s}{2V_{dc}} \end{bmatrix} \begin{bmatrix} -\left(\sqrt{3}-2\right) & -1 \\ \left(\sqrt{3}-1\right) & -\left(\sqrt{3}-1\right) \\ 1 & \left(\sqrt{3}-2\right) \\ 0 & 2 \end{bmatrix} \begin{bmatrix} V_{sd}^* T_s \\ V_{sq}^* T_s \\ 0 \\ 0 \end{bmatrix} = \begin{bmatrix} -T_1 \\ -T_6 \\ T_3 \\ T_4 \end{bmatrix} \tag{23}$$

Equation (23) is used to determine the dwell time constants for sector 1 and based on that the modulating signal is obtained. Further, for the generation of gate pulses, two carrier waves of 180^0 phase shift are employed. For the sectors (3,4,7,8,11,12,15,16,19,20,23,24), the carrier wave with 0^0 phase shift and in sectors (1,2,5,6,9,10,13,14,17,18,21,22), the carrier wave with 180^0 phase shift are used. The flowchart for the proposed research methodology has been depicted in Figure 4 below.

4. Results and discussion

The Simulink model of modified SVM technique with IRFOC of SPAIM is developed using Simulink toolbox of MATLAB software and a prototype model of SPAIM drive rated for 2 HP, 4-pole, 200V machine is developed for the validation of the control algorithm. The effectiveness of the proposed algorithm is investigated through simulation studies under various operating conditions and validated through tested results obtained from prototype mode as depicted in Figure 5 to Figure 12.

4.1. Simulation results

The simulation study for the developed Simulink model is carried out and its performances are investigated as depicted in Figure 5 to Figure 7. Figure 5 represents the waveforms of stator phase currents, torque, speed, and
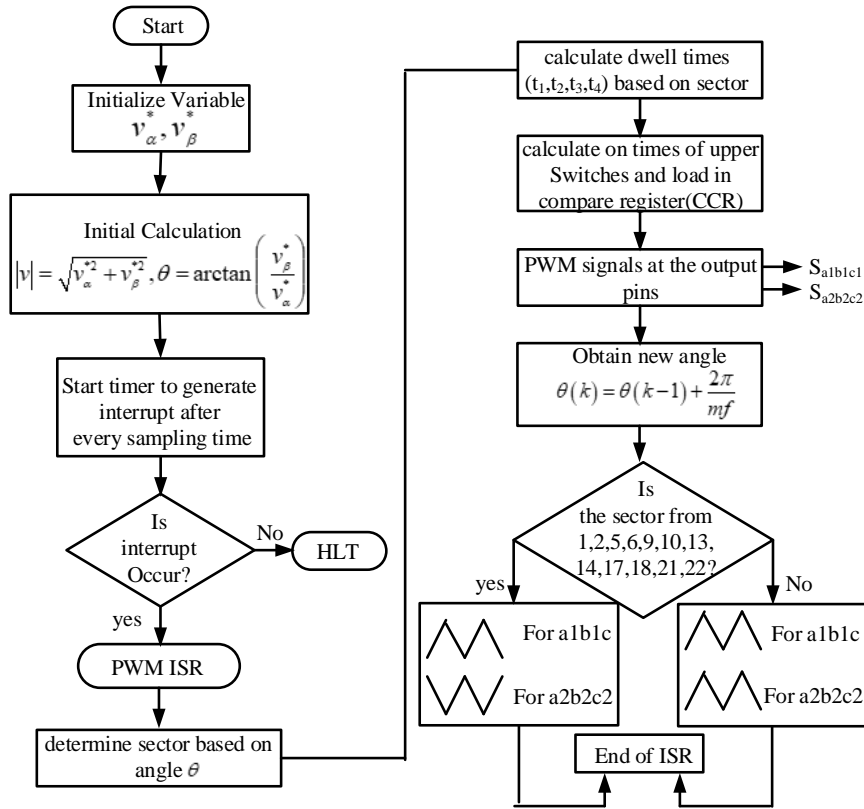
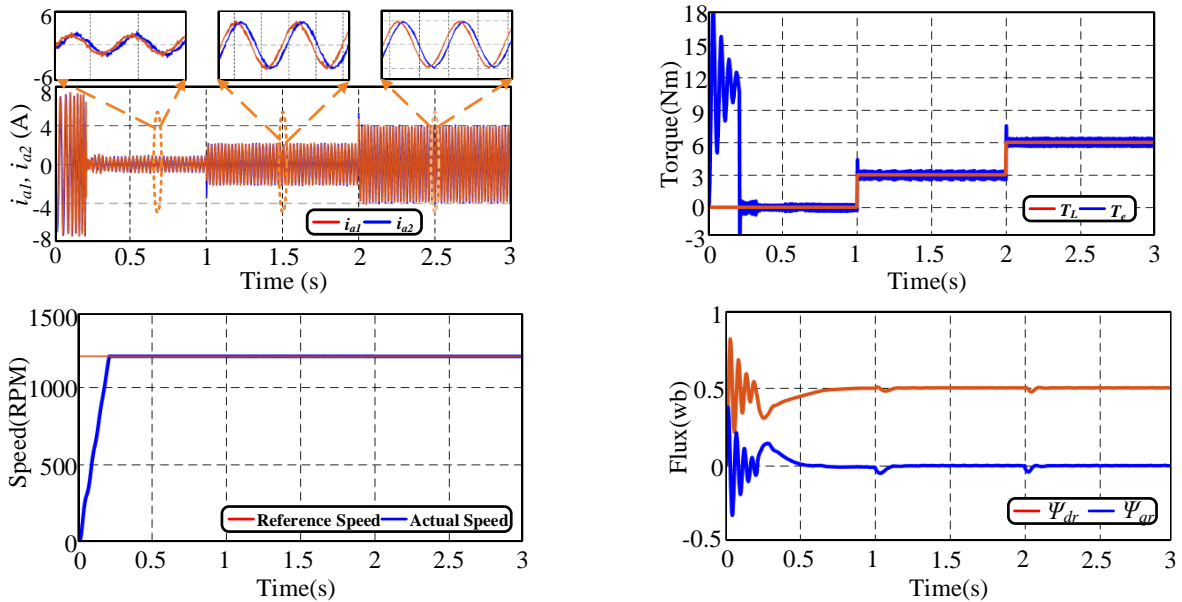**Figure 4**. Flowchart of proposed methodology.

Figure 5. Simulation results of SPAIM drive with modified SVM technique for the reference speed of 1200 rpm and dynamic load variation (a) phase currents (i_{a1}, i_{a2}) (b) torques (T_L, T_e) (c) speed (d) rotor fluxes (ψ_{dr}, ψ_{qr}).

d-axis and q-axis rotor fluxes for different load conditions. It is observed in Figure 5 that the reference speed is kept constant at 1200 rpm throughout the operation. Initially, the machine starts with light load condition, and at time instant t = 1s, the load is increased to half load condition i.e 3 Nm, and at time instant, t = 2s, the load is further increased to full load i.e 6 Nm. From the results, it is clear that the reference speed is accurately tracked by the actual speed irrespective of load conditions. The magnitude of the d-axis and q-axis rotor flux is 0.5wb (rated value) and 0wb respectively, which represent the proper field orientation. The stator current distortion in terms of percentage THD for half-load and full-load conditions is 4.5% and 3%, respectively and torque ripple is the same as 0.12 Nm for half-load and full-load conditions.

In order to investigate the performance of the modified SVM technique with SPAIM drive under dynamic conditions, the step change in speed keeping constant load is carried out and test results are obtained as depicted in Figure 6. The load on the machine is kept constant at 6 Nm throughout the operation. The machine starts with a reference speed of 1000 rpm and t = 1.5s; the reference speed is changed to 1400 rpm. The simulation results show that the actual speed smoothly tracks the reference speed under abovesaid variations. The q-axis rotor flux is equal to 0, which represents proper flux orientation. The percentage distortion in the stator currents is 2% which is very small compared to the conventional vector control technique.
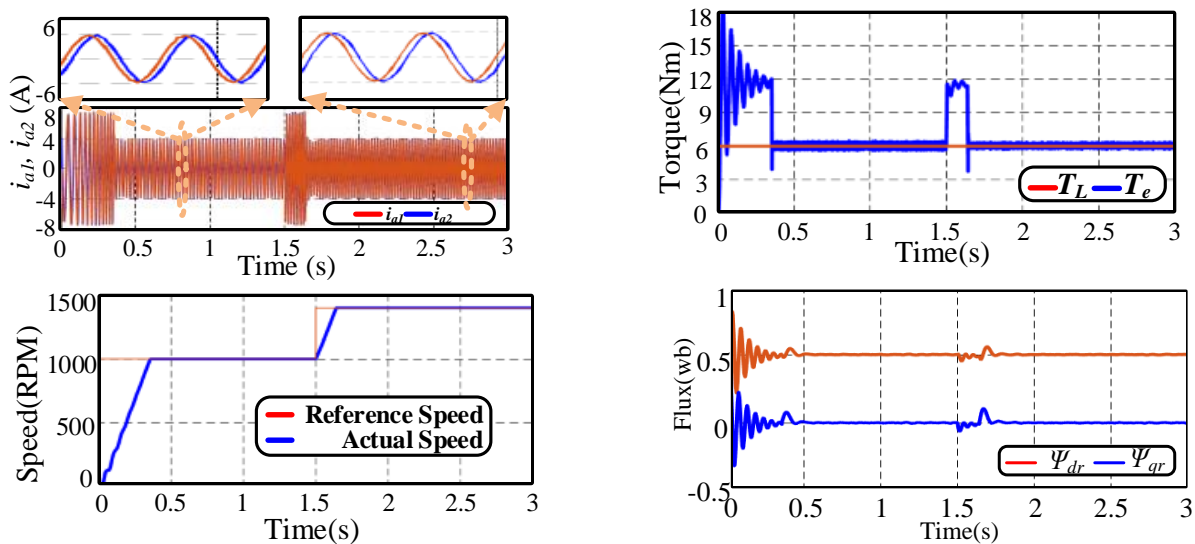

Figure 6. Simulation results of SPAIM drive with modified SVM technique for the constant load of 6Nm and dynamic load variation: step change from 1000 rpm to 1400 rpm (a) stator phase currents (i_{a1}, i_{a2}) (b) torques (T_L, T_e) (c) speed (d) rotor fluxes (ψ_{dr}, ψ_{qr}).

The proposed SVM technique is further simulated and tested under speed reversal. In this case, the SPAIM starts with a reference speed of 100 rpm initially, and at t = 1.5s, the speed command is changed to -100 rpm. It is observed in Figure 7 that the reversal of reference speed is tracked by actual speed accurately. The orientation of rotor flux is proper, and distortion in the stator current is low of the order of 3.75%.

4.2. Test results

The modified SVM-based IRFOC for SPAIM has been implemented using TMS320F28379D controller board with a sampling rate of 100 µs. The detailed parameters of prototype SPAIM have been listed in Appendix. The CTs based current sensors have been used to sense the stator phase currents. The isolation circuit is used

to amplify the PWM pulses generated by controller before feeding to the six-leg VSC. The optical encoder with 1024 ppr is used for the measurement of rotor speed. The photograph of the hardware prototype test setup of the proposed system is shown in Figure 8. The test results are presented in the following subsections.
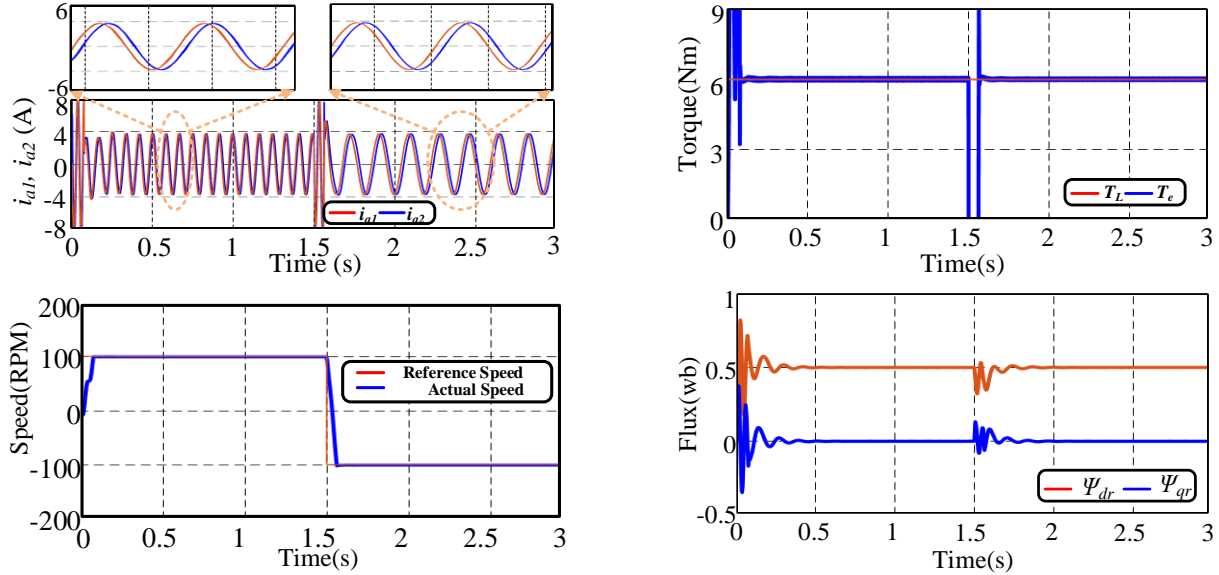

Figure 7. Simulation results of SPAIM drive with modified SVM technique for the constant load of 6Nm and dynamic load variation: step change from 100 rpm to -100 rpm (a) stator phase currents (i_{a1}, i_{a2}) (b) torques (T_L, T_e) (c) speed (d) rotor fluxes (ψ_{dr}, ψ_{qr}).
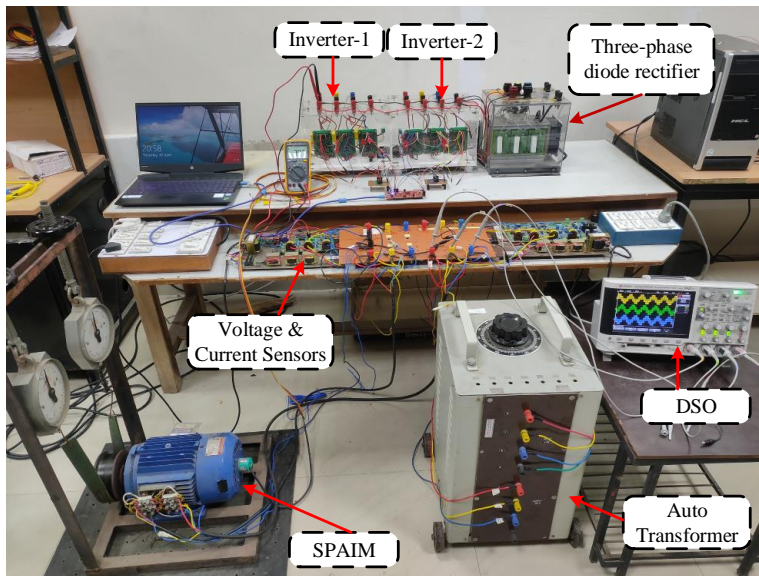

Figure 8. Experimental test setup

The experimental results for stator currents (i_{a1}, i_{a2}), along with the harmonic spectrum of phase current (i_{a1}), have been represented in Figure 9(a)-(b) for a half load and full load conditions respectively. As shown in the figure, the results are recorded with 10ms/div. Stator's current scale is set to 3A/div. The span for the

harmonic spectrum is 20kHz, with its center at 9.6kHz. It is observed that the distortions in stator currents in terms of percentage total harmonic are 5.5% and 6.75% for half-load and full-load conditions which is significantly low as compared to benchmarked SPWM, and hysteresis control techniques.

The proposed algorithm is also investigated under different operating conditions. Initially, the motor starts under light load condition and the load is gradually increased to 3 Nm and 6 Nm. The obtained test results are presented in Figure 10 which represents the experimental results of phase voltage (v_{a1}, v_{a2}), phase current (i_{a1}, i_{a2}), and $\alpha - \beta$ current with constant speed command of 1000 rpm and dynamic load variation. Further, in Figure 10, the expanded views are also depicted for different load conditions. The current and voltage scales are set to 6 A/div and 100 V/div, respectively.
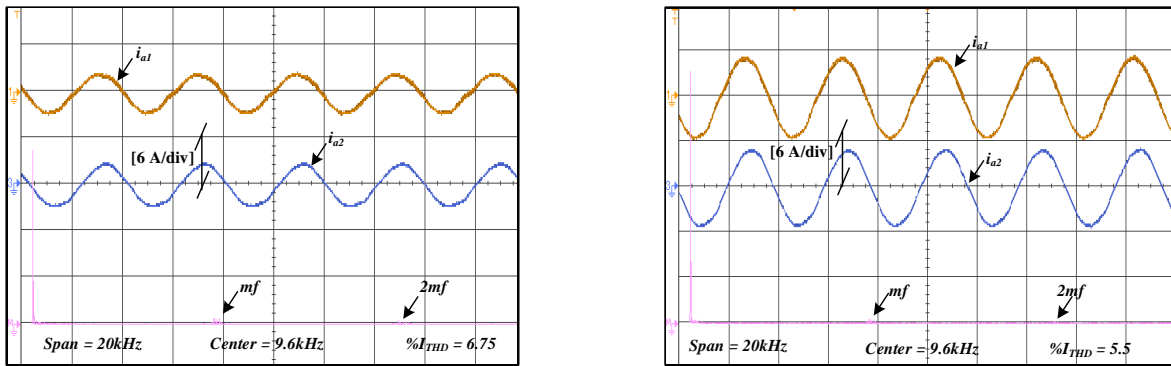

Figure 9. Waveforms of stator currents (i_{a1}, i_{a2}) and harmonics spectra of (i_{a1}) of prototype SPAIM drive with modified SVM technique under different loading conditions (a) half-load (b) full-load.
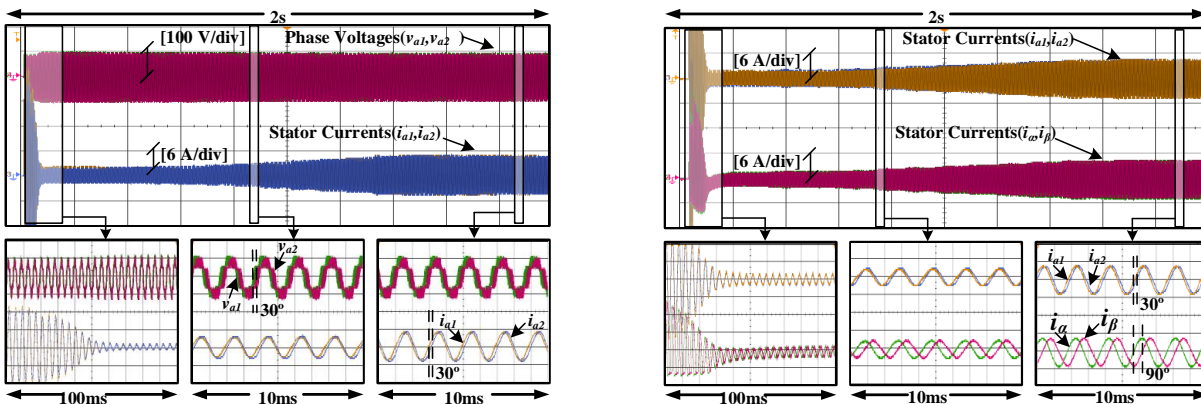

Figure 10. Voltage and current waveforms of prototype SPAIM drive with modified SVM technique for the speed of 1000 rpm and dynamic load variation (a) stator phase voltage (v_{a1}, v_{a2}) and phase current (i_{a1}, i_{a2}) (b) stator currents in $\alpha - \beta$ subspace (i_{α}, i_{β}) .

The test results of actual speed, rotor position, and stator phase currents (i_{a1}, i_{a2}) for constant speed and dynamic load variation have been depicted in Figure 11(a). The motor was started with a reference speed of 1000 rpm and light load condition. After that, the loading was gradually changed to full load condition. The expanded views of initial transients, light load condition, and full load condition have also been represented. The current scale is set to 6 A/div. The speed and rotor position scales are set to 1000rpm/div and 6.28

rad/div. The results clearly show that the actual speed is maintained constant at 1000 rpm irrespective of load condition.

Figure 11(b) represents experimental results of actual speed, rotor position, and phase currents (i_{a1}, i_{a2}) for constant load and dynamic speed variation. Initially, the machine starts with a speed command of 1000 rpm and after that, the reference speed is gradually increased to 1200 rpm. During this operation, the load has been kept constant. From the results, it is clear that the speed transition has been tracked smoothly by the actual speed. The expanded views for initial transients, 1000 rpm speed command, and 1200 rpm speed command have been presented.
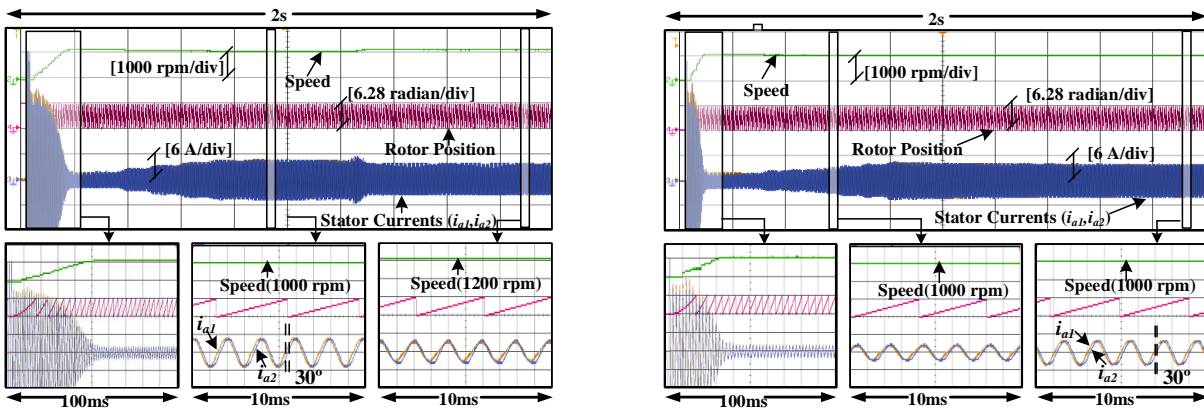

Figure 11. Waveforms of actual speed, rotor position, and stator phase currents (i_{a1}, i_{a2}) of prototype SPAIM drive with modified SVM technique under (a) constant speed 1000 rpm and dynamic load variations (b) constant load and speed variations.

5. Comparetive performance analysis

In this section, the performance of the modified SVM-based IRFOC SPAIM drive is compared with benchmarked SPWM and hysteresis-based rotor field-oriented control in terms of stator current distortion (% THD), torque ripples, and computational complexity. Figure 12 represents stator currents of phases a1 and a2 with SPWM and hysteresis current control with constant speed reference of 1200 rpm and dynamic load variation. The stator current distortion (% THD) is 12 % and 22.18 % respectively for SPWM and hysteresis current control under full load conditions, which is very high compared to that of modified SVM technique. The different techniques for IRFOC of the SPAIM drive have been compared in terms of stator current THD, torque ripples, and computational complexity in Table 3.
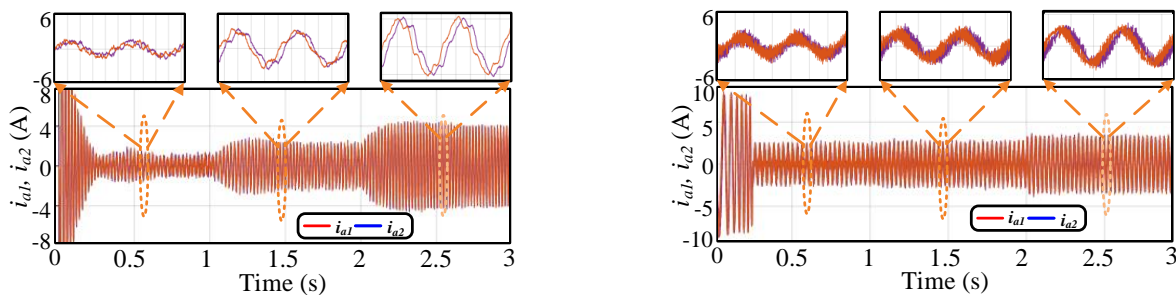

Figure 12. Simulated waveforms of stator phase currents (i_{a1}, i_{a2}) of SPAIM drive with a constant speed of 1200 rpm and dynamic load variations under different techniques (a) SPWM (b) Hysteresis control.

It is evident that the proposed SVM technique offers better performance in terms of stator current distortion and torque ripples. The analysis of stator current distortion ($\%I_{THD}$) with hysteresis control, SPWM, and modified SVM methods under variable load conditions is depicted in Figure 13 and it shows that the modified SVM technique provides the least stator current distortion under a wide range of load conditions, from no load to full load.

Table 3. Comparative performance analysis.

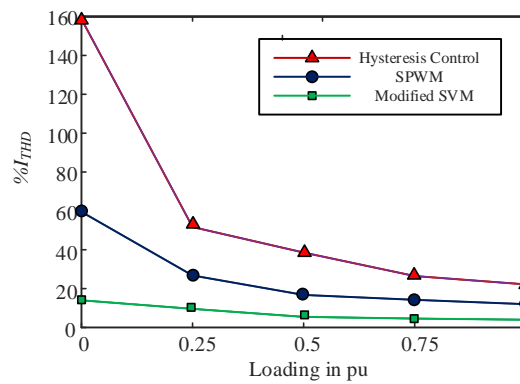| IRFOC Method	Stator current THD	Torque ripple	Computational complexity
Modified SVM	4.00	0.12	High
SPWM	12.60	0.20	Moderate
Hysteresis controller	25.10	0.25	Low

Figure 13. Analysis of stator current distortion ($\%I_{THD}$) under different load conditions.

6. Conclusion

This paper elaborates IRFOC of SPAIM drive using a modified carrier wave-based SVM technique. The mathematical modelling of SPAIM is carried out in a synchronously rotating reference frame to emulate DC motor control features. The utilization of modified SVM scheme improves the steady state and dynamic performance of SPAIM drive in terms of distortion of stator currents and torque ripples to a great extent. The reduction in stator current is achieved by the appropriate selection of switching sequence with a proper combination of large, medium, and zero switching vectors and carrier waves in each sector. The complete procedure of selection of switching sequences for the first four sectors is explained and based on that the same can be obtained for the remaining sectors. The calculation of dwell times for sector-1 is also narrated in detail and the same procedure can be followed to calculate the dwell times for the remaining sectors. This scheme can be extended to any number of phases which are multiple of three as the machine's model is based on two axes $(d-q)$. This scheme is easy to implement in practice. The performance of the proposed algorithm is tested in all the possible operations and speed ranges using simulation studies using MATLAB/Simulink as well as experimentation with help of TMS320F28379D Controller board. Based on simulation studies and experimentation, it is found that the performance of a multi-phase induction motor is very satisfactory for electric vehicle applications.

Appendix

The parameters of six-phase induction motor are as follows: Ratings: 1.5 kW, 200 V, 50Hz, stator resistance (R_s): 4.35 Ω, rotor resistance (R_r): 4.61Ω, stator leakage inductance (L_{ls}): 0.01153 H, rotor leakage inductance (L_{lr}):0.02211 H, Magnetizing Inductance (L_m): 0.430 H, Pole pairs (P): 4, Rotor inertia (J): 0.05 kg-m2.

References

[1] Bose BK. Modern Power Electronics and AC Drives. Upper Saddle River, NJ, USA: Prentice Hall, 2002.

[2] Krishnan R. Electric Motor Drives – Modeling, Analysis and Control. Upper Saddle River, NJ, USA: Prentice Hall, 2013.

[3] Krause PC, Wasynczuk O, Sudhoff S, Pekarek S. Analysis of Electric Machinery and Drive Systems. New York,NY, USA: Wiley, 2013

[4] Levi E, Bojoi R, Profumo F, Toliyat HA, Williamson S. Multiphase induction motor drives - a technology status review. IET Electric Power Applications 2007;1 (4): 489-516. https://doi.org/10.1049/iet-epa:20060342

[5] Singh G. Multi-phase induction machine drive research—a survey. Electric Power Systems Research 2002; 61 (2): 139-147. https://doi.org/10.1016/S0378-7796(02)00007-X

[6] Zhao Y, Lipo TA. Space vector PWM control of dual three-phase induction machine using vector space decomposition. IEEE Transactions on Industry Applications 1995; 31 (5): 1100-1109. https://doi.org/10.1109/28.464525

[7] Levi E. Multiphase Electric Machines for Variable-Speed Applications. IEEE Transactions on Industrial Electronics 55 (5): 1893-1909. https://doi.org/10.1109/TIE.2008.918488

[8] Barrero F, Duran MJ. Recent Advances in the Design, Modeling, and Control of Multiphase Machines—Part I. IEEE Transactions on Industrial Electronics 2016; 63 (1): 449-458. https://doi.org/10.1109/TIE.2015.2447733

[9] Duran MJ, Barrero F. Recent Advances in the Design, Modeling, and Control of Multiphase Machines—Part II. IEEE Transactions on Industrial Electronics 2016; 63 (1): 459-468. https://doi.org/10.1109/TIE.2015.2448211

[10] Suhel SM, Maurya R. Modelling, design and analysis of multi-phase induction motor. International Journal of Power and Energy Conversion 2017; 8: 186-203. https://doi.org/10.1504/IJPEC.2017.10002908

[11] Marouani K, Baghli L, Hadiouche D, Kheloui A, Rezzoug A. A New PWM Strategy Based on a 24-Sector Vector Space Decomposition for a Six-Phase VSI-Fed Dual Stator Induction Motor. IEEE Transactions on Industrial Electronics 2008; 55(5): 1910-1920. https://doi.org/10.1109/TIE.2008.918486

[12] Suhel SM, Maurya R. Realization of 24-Sector SVPWM With New Switching Pattern for Six-Phase Induction Motor Drive. IEEE Transactions on Power Electronics 2019; 34 (6): 5079-5092. https://doi.org/10.1109/TPEL.2018.2870952

[13] Suhel SM, Maurya R. Simplified implementation of SVPWM techniques for a six-phase machine with reduced current distortion features. IET Electric Power Applications 2019; 13 (11): 1053-1063. https://doi.org/10.1049/iet-epa.2018.5918

[14] Pandit JK, Aware MV, Nemade R, Tatte Y. Simplified Implementation of Synthetic Vectors for DTC of Asymmetric Six-Phase Induction Motor Drives. IEEE Transactions on Industry Applications 2018; 54 (3): 2306-2318. https://doi.org/10.1109/TIA.2018.2789858

[15] Suhel SM, Maurya R, Gupta N. Modified switching table based direct torque control of six phase induction motor drive. Electric Power Components and System 2019; 47 (12): 1077-1089. https://doi.org/10.1080/15325008.2019.1637970

[16] Shao B, Zhu ZQ, Feng J, Guo S, Li Y et al. Compensation of Selective Current Harmonics for Switching-Table-Based Direct Torque Control of Dual Three-Phase PMSM Drives. IEEE Transactions on Industry Applications 2021; 57(3): 2505-2515. https://doi.org/10.1109/TIA.2021.3059190

[17] Pandit JK, Aware MV, Nemade R, Levi E. Direct Torque Control Scheme for a Six-Phase Induction Motor With Reduced Torque Ripple. IEEE Transactions on Power Electronics 2017; 32 (9): 7118-7129.https://doi.org/10.1109/TPEL.2016.2624149

[18] Bojoi R, Lazzari M, Profumo F, Tenconi A. Digital field-oriented control for dual three-phase induction motor drives. IEEE Transactions on Industry Applications 2003; 39 (3): 752-760. https://doi.org/10.1109/TIA.2003.811790

[19] Singh GK, Nam K, Lim SK. A simple indirect field-oriented control scheme for multiphase induction machine. IEEE Transactions on Industrial Electronics 2005; 52 (4): 1177-1184. https://doi.org/10.1109/TIE.2005.851593

[20] Alehifar M, Arashloo RS, Moreno-Eguilaz M, Sala V, Romeral L. Observer based open transistor fault diagnosis and fault tolerant control of five-phase permanent magnet motor drive for application in electric vehicle. IET Power Electronics 2015; 8 (1):76–87. https://doi.org/10.1049/iet-pel.2013.0949

[21] Jones M, Vukosavic SN, Dujic D, Levi E. A Synchronous Current Control Scheme for Multiphase Induction Motor Drives. IEEE Transactions on Energy Conversion 2009; 24 (4): 860-868. https://doi.org/10.1109/TEC.2009.2025419

[22] Rubino S, Dordevic O, Bojoi R, Levi E. Modular Vector Control of Multi-Three-Phase Permanent Magnet Synchronous Motors. IEEE Transactions on Industrial Electronics 2021; 68 (10): 9136-9147. https://doi.org/10.1109/TIE.2020.3026271

[23] Sala G, Mengoni M, Rizzoli G, Zarri L, Tani A. Decoupled d–q Axes Current-Sharing Control of Multi-Three-Phase Induction Machines. IEEE Transactions on Industrial Electronics 2020; 67 (9): 7124-7134. https://doi.org/10.1109/TIE.2019.2941127

[24] Holakooie MH, Iwanski G. An Adaptive Identification of Rotor Time Constant for Speed-Sensorless Induction Motor Drives: A Case Study for Six-Phase Induction Machine. IEEE Journal of Emerging and Selected Topics in Power Electronics 2020; 9 (5):5452-5464. https://doi.org/10.1109/JESTPE.2020.3042305

[25] Rubino S, Bojoi IR, Mandrile F, Armando E. Modular Stator Flux and Torque Control of Multi-Three-Phase Induction Motor Drives. IEEE Transactions on Industry Applications 2020; 56 (6):6507-6525. https://doi.org/10.1109/TIA.2020.3022338